# Tilted illumination in-line holographic velocimetry: improvements in the axial spatial resolution

Julia Lobera*, Virginia Palero, Eva Roche, Marina Gómez Climente, Ana M. López Torres, Nieves Andrés, M. Pilar Arroyo

Instituto de Investigación en Ingeniería de Aragón (I3A), Universidad de Zaragoza, Zaragoza, Spain.
*Correspondent author: jlobera@unizar.es

## Abstract

Two are the main limitations of in-line holography: the twin image problem and the poor spatial resolution in the optical axis direction. The twin image problem can be solved with the introduction of an imaging lens and a knife-edge aperture located at its focal plane. In this work, a theoretical analysis of the axial resolution with and without aperture is provided from the perspective of the Optical Diffraction Tomography. Theoretical analysis and controlled experiments with the different recording options, demonstrate that a small tilt of the illumination beam, together with a centered rectangular aperture, is a key parameter as it improves the spatial resolution along the optical axis during the location and tracking of a particle field.

## 1. Introduction

Digital in-line holography (DIH) is a powerful three-dimensional (3D) imaging technique with a wide range of applications. In fluid velocimetry, DIH allows locating and tracking particles, and, combined with Particle Image Velocimetry or Particle Tracking Velocimetry, allows simultaneous 3C-3D velocity measurements in a flow [1-4]. Two are the main limitations of DIH in particle velocimetry: the twin image problem and the poor spatial resolution in the optical axis direction [5, 6, 7].

The analysis of the particle field shows that the presence of the twin-image has little influence on the measured particle position but underestimates the small out-of-plane displacements [8, 9]. Several approaches have been proposed to eliminate or minimize the twin image. Most of them include several recordings that are not suitable for dynamic measurements. Other solutions require certain limitations in the object frequency bandwidth, size, or sparsity. A detailed analysis of these methods, along with an iterative deconvolution procedure, can be found in Denis et al [10]. In this paper, we do chose to remove one of the images completely by an appropriate recording setup. Bryngdahl et al [11] proposed, in the early days of the holography, the use of an imaging lens and a knife-edge aperture on its focal plane. More recently, this approach has been applied for 3D PTV with digital holography [9, 12], and it has been used to determine the 3D velocity field on a carotid bifurcation model [13].

Any aperture in the focal plane reduces the available laterals frequencies, and therefore

the lateral resolution. However, the effect on the axial resolution is not so straightforward, as it also depends on the illumination and observation directions, as will be detailed in section 3.

Nevertheless, the main limitation in the accuracy of the measured 3D velocity field is the correct location and tracking of the particle along the optical axis direction. Some notable works are contributing to improve the axial resolution, either modifying the reconstruction process [14, 15] or the recording set-up. To improve the spatial resolution, tomography combines the object information obtained with several illumination or/and observation directions [16,17], which usually implies complicated set-ups with many cameras and a cumbersome calibration and image analysis.

To simplify the tomographic system, several recordings can be taken simultaneously with one camera. Multiple in-line holography requires introducing a small tilt of the illuminating beams [18-20]. The observed particle scattering depends on the illumination beam direction and thus, different parts of the off-axis scattering are recorded. Previous works [21-23] have proved the relevance of a proper recording and wise use of the off-axis particle scattering even with a DIH configuration. Thus, the effect of tilting the illuminating beam should be considered by itself and this is the main objective of the present work.

In this paper, the performance of a DIH set-up for the measurement of the 3D position and displacement of a dense particle field will be investigated. Particularly, we will focus on the axial resolution improvement. For this purpose, we will compare different configurations: with and without aperture; with parallel and tilted illumination; and a double multiplexed recording. We will provide a theoretical analysis of the recorded axial object frequencies and controlled experiments of a particle field for each configuration. It will be proved that a rectangular aperture combined with a tilted illumination outperforms the other options.

## 2. DIH configurations

Figure 1a shows a particle field (object) illuminated with a collimated beam parallel to the optical axis, henceforth parallel illumination (PI). A lens is used to image the particle field at a plane near the digital sensor. As the particles are slightly out of focus at the hologram plane, the particle diffraction pattern is recorded. The lens allows modifying the magnification and therefore to adjust the recorded field of view to the region of interest. Moreover, an aperture can be located at the focal plane of the imaging lens to remove the twin-image [9].

The imaging lens provides access to the object lateral frequencies $(\xi, \eta)$, whose maxima values are determined by the sensor pixel size. A scheme of the focal plane is shown in figure 1b, where the recordable frequencies according to the Nyquist criterion are in grey. Usually, the lens diameter does not limit the resolution of the imaging system, and the numerical aperture $NA = sin(\sigma)$ is determined by the pixel size, whose relation with the spatial frequencies will be detailed in section 3. The green dot shows the location of the focused illuminating beam and the rectangular aperture is highlighted in white, which select the recorded frequencies.

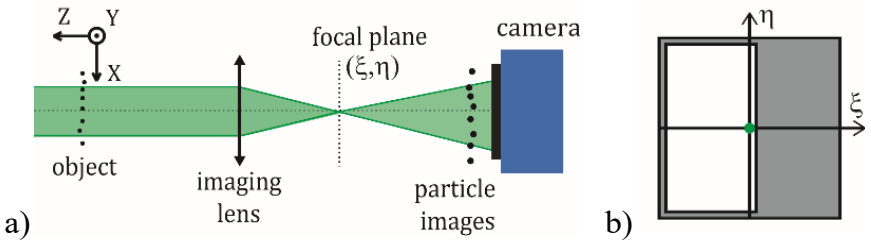


Fig. 1. Top view of the parallel illumination (PI) configuration (a) and the transversal view of the aperture position on the focal plane (b).

Each hologram is the recording of the interference between the scattered beam that reaches the sensor, which defines the observation direction, and the non-scattered illuminating beam. Thus, the ability to record the 3D scatterer (particle) positions is determined by the sensitivity vector defined in Holographic Interferometry [6, 7] as $\boldsymbol{K} = \boldsymbol{k_o} - \boldsymbol{k_i}$, where $\boldsymbol{k_o}$and $\boldsymbol{k_i}$ are the wave vectors along the observation and illumination directions. For a DIH configuration, in the object space, the illumination wave vector is parallel to the optical axis and the observation wave vectors will fill the solid angle defined by the numerical aperture of the system. The sensitivity vector axial component is close to zero, with the consequence of a limited axial resolution. A tilted illumination (TI) will change $\boldsymbol{k_i}$ and therefore the axial spatial resolution, as will be explained in the following.

Figure 2 shows a tilted illumination (TI) set-up and the XY view of the aperture position on the focal plane. In this case, the illumination is tilted at an angle $\theta \cong \sigma/2$. The rectangular aperture is centered on the optical axis, so that the illuminating beam is focused near one edge of the rectangular aperture.

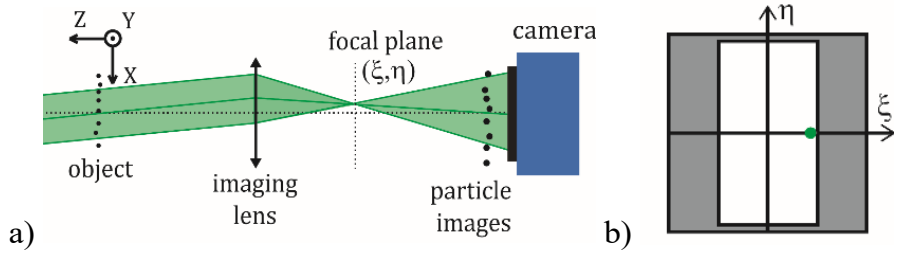


Fig. 2. Top view of the tilted illumination (TI) configuration (a) and the transversal view of the aperture position on the focal plane (b).

In both cases, for parallel and tilted illumination, the aperture modifies the particle images in a similar way. Figure 3a-b) shows an area of 250x250pixels of a typical hologram recorded with a TI configuration without aperture (WA) and with a rectangular aperture (RA), i.e. TIWA and TIRA cases respectively. The particle images are recorded slightly defocused to avoid pixel locking. The aperture reduces the scattering pattern of each particle to half of the typical scattering pattern.

a) 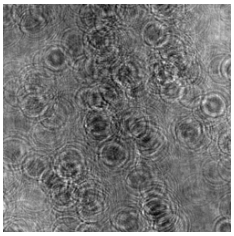 b) 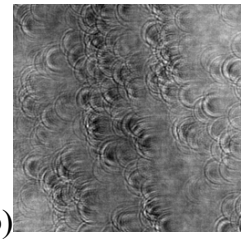 c) 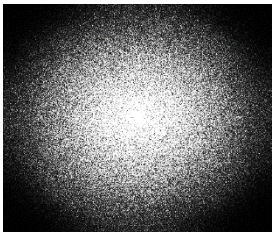 d) 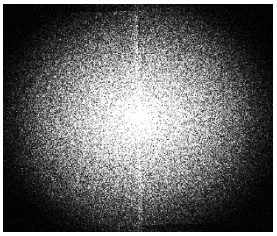

Fig. 3 Particle images at the hologram plane for TIWA (a) and TIRA (b) configuration. Fourier Transform of typical TIWA (c) and TIRA (d) holograms.

With a small angle tilted illumination set-up, the reconstructed 3D particle images have a typical cigar shape, whose intensity distribution is not centered along the optical axis but along the illumination direction. The main difference of the particle images with parallel or tilted illumination is that the particle images appear laterally shifted at any plane different from their in-focus plane.

Figure 3c-d) shows the frequency spectrum intensity of a TIWA hologram and a TIRA hologram. The introduction of the aperture allows separating on the frequency spectrum the two interference terms responsible of the twin images (figure 3d). These are the virtual and real images of the object at the aperture plane [9, 13]. The two images are just overlapped near the zero frequencies in the $\xi$-direction (bright vertical line in Figure 3d), as the illumination beam must be recorded. This separation of the interference terms is the key advantage of the side-band holography as has been proved by Bryngdahl et al. 1968.

From a different perspective, the recording can be considered as a lensless Fourier hologram of the object beam at the plane of the aperture. In such a case, the reference or illuminating beam is a divergent wave that comes from the focal plane centre (Fig. 1a). The object beam comes from any point of the aperture, which is in the same plane as the source of the reference beam. Therefore, a Fourier transform of the hologram will provide two object images symmetrically shifted from the centre of the spectrum [5, 7]. The tilt of the illumination will modify the mean propagation direction of the reference, but it will not have any effect on the aperture image position on the Fourier Transform. For PIRA and TIRA configurations, the reference source is perfectly adjusted to be at the edge of the aperture. Thus, both aperture images will appear so close that they may seem one continuous spectrum. Only when misaligned, both contributions will be apparent [9]. When the object is not restricted with an aperture, there will be points at both sides of the reference origin. Therefore, the real and virtual images will be completely overlapped when the hologram is reconstructed with a Fourier Transform. On the TIWA spectrum (Figure 3c), the twin images cannot be distinguished. The particle images and the frequency spectrum of the holograms recorded with the parallel illumination set-up are very similar to those on figure 3 and they cannot be visually distinguished.

For a multiplexed recording, a double-tilted illumination (DTI) is used. Two collimated beams, with incidence angles set to $\pm\sigma/2$ and crossed polarizations, illuminate the particle field. Without aperture, the different interference terms will be overlapped at any plane. A rectangular aperture allows the two interference terms coming from the same hologram, to be separated, but not from the crossed terms due the second multiplexed hologram. We could

reduce the aperture in order to separate completely the four interference terms in the frequency spectrum. For this reason, a square aperture (SA), with half-size of the rectangular aperture used previously, is also considered. It should be centered on the $\xi$-axis and shifted vertically from the optical axis as shown in figure 4a. Figure 4b shows the Fourier Transform of a hologram. The corresponding images from the illumination 1 appears at the quadrants labeled as 1a and 1b, and the images from the other illumination at the quadrants 2a and 2b. Thus, holograms recorded with both illuminations can be analyzed separately. In the hologram plane, each particle produces two shifted defocused images, which are cut off by the aperture, showing each a different quarter of the scattering pattern (fig 4c).

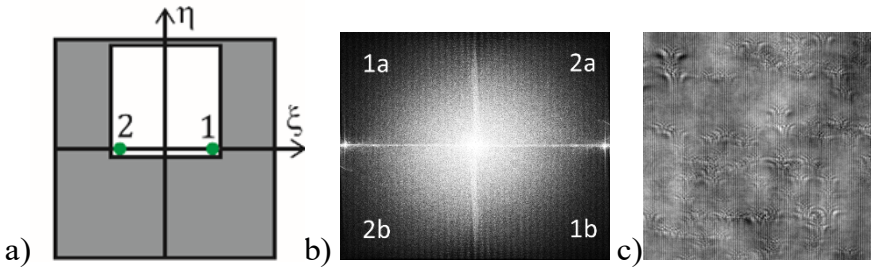


Fig. 4. DTISA configuration: (a) transversal view of the aperture position on the focal plane, (b) hologram frequency spectrum intensity and (c) particle images at the hologram plane

## 3. Spatial resolution analysis

The use of an aperture, and therefore only part of the available frequencies, reduces the lateral resolution. However, the effect on the axial resolution is not so straightforward. To understand its influence we will describe each recording system with an interferometric approach, where the sensitivity vector is the relevant parameter.

A holographic reconstruction provides an estimate of the variations in the object refractive index, i.e. the scattering potential defined as $\Phi(\mathbf{r}) = -k^2\left(n^2(\mathbf{r})-1\right)$ , where $k = 2\pi/\lambda$ , and λ is the free space wavelength. Within the scalar diffraction theory, the spectral components of the reconstructed object beam, $U(K_x,K_y,K_z)$, can be directly related to the scattering potential [24-26]. However, only the spectral components defined by the sensitivity vector can be measured. Consequently, the scattered field by the object is a linear filtered measurement of the scattering potential [16].

$$U(K_x,K_y,K_z) \propto \int \Phi(\mathbf{r}')\exp(-i\mathbf{K}\cdot\mathbf{r}')d\mathbf{r}' \qquad \textbf{(1)}$$

The illumination wave vector $\mathbf{k_i}$ and all the plane wave components of the measured scattered field (observation wave vectors $\mathbf{k_o}$) can be represented on a sphere shell of radius k, as only propagating waves can be recorded at the far field. Figure 5 top, illustrates the range of the observation $\mathbf{k_o}$ (in green) and the illumination $\mathbf{k_i}$ wave vectors for an in-line recording set-up at the YZ and XZ sections. The $\mathbf{k_i}$ presents an incidence angle of θ=0 for parallel illumination (figure 5a and 5b) and around θ=σ/2 for tilted illumination (figure 5a and 5c). The rectangular aperture reduces the observation directions, which are highlighted in dark

green. The sensitivity vectors, and therefore, the measurable spatial frequencies of the scattering potential can be found by shifting the $\mathbf{k_o}$ shell according to $\mathbf{K}=\mathbf{k_o}-\mathbf{k_i}$ (figure 5, bottom).

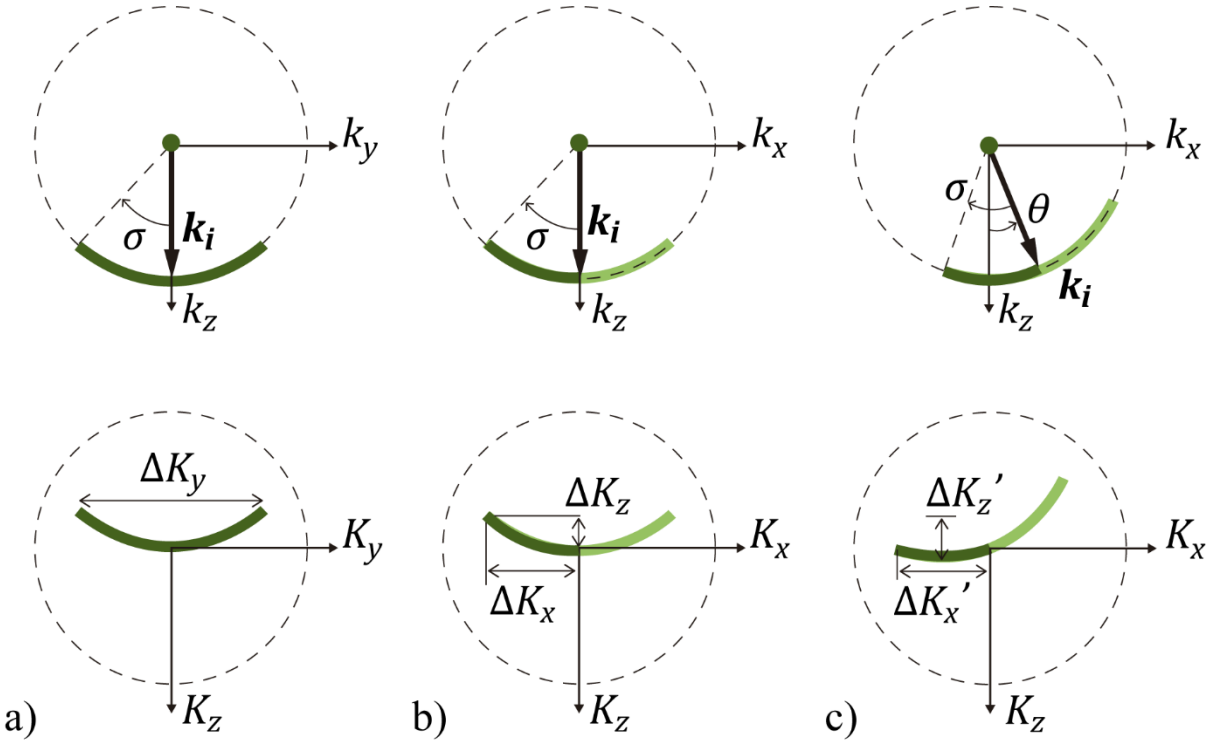


Fig. 5. Illumination and observation wave vectors (top) and corresponding sensitivity vector (bottom): a) YZ section; b) XZ section for PI; c) XZ section for TI.

The spatial resolution can be estimated, according to the Nyquist criterion, as the shortest spatial period that can be resolved corresponding to a certain frequency bandwidth [16, 27], which can be related to the range of the sensitivity vector since $K_x = 2\pi\xi$ and $K_y = 2\pi\eta$. The range of the sensitivity vector in the three directions are shown at figure 5 (bottom), from which the spatial resolution can be calculated. For instance, the lateral resolution for the Y direction (figure 5a) is:

$$R_y = \frac{2\pi}{\Delta K_y} = \frac{\lambda}{2\sin(\sigma)} \qquad \textbf{(2)}$$

In practice, the lens size is usually big enough so that the lateral spatial resolution is really limited by the pixel size ($pix$). The pixel size in the object space determines σ, and therefore the spatial resolution in the different configurations. Without aperture, $R_y = R_x = 1pix$ which determines the measurable spatial frequencies $(\xi, \eta)$ and the lateral sensitivity vector range. Consequently, the measurable observation directions must be close to the illumination direction, which is particularly relevant in the case of a tilted illumination. With a rectangular aperture $R_y = 1pix$ and $R_x = 2pix$, for both PI and TI cases.

The difference is found in the axial component, $K_z$, which can be determined once the range of the observation direction is known. The measurable $\boldsymbol{K}$ vectors are distributed on a

sphere and only two sections are represented in figure 5. To improve the visualization of the axial components, we computed the corresponding $K_z$ for each spatial frequency of the spectrum $(\xi, \eta)$. We have mapped $K_z$ for $pix = 3\mu m$ (in the object space) and λ=515nm for PI (figure 6a) and TI (figure 6b). The lateral spatial frequencies range from -0.5/pix to 0.5/pix. The region recorded with the rectangular aperture is framed in black.

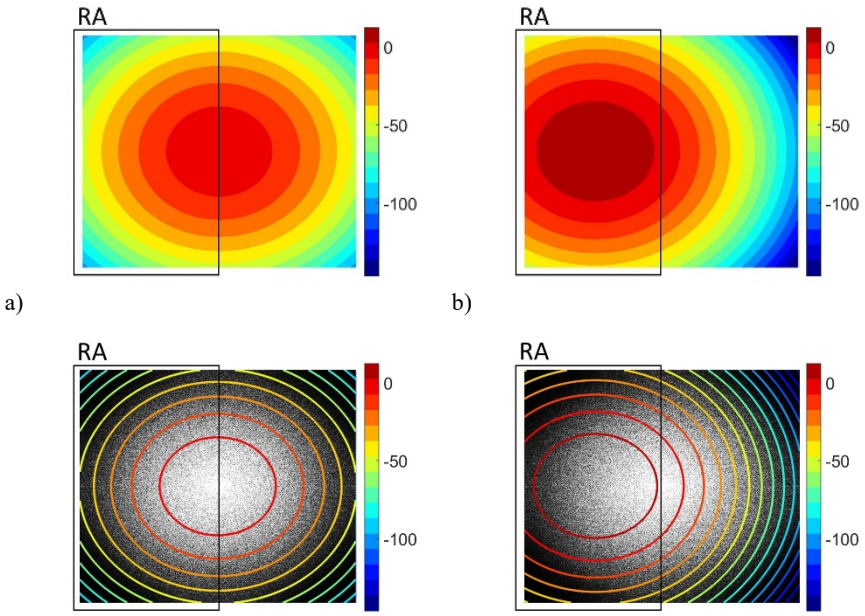


Fig. 6. Map of $K_z$ $(mm^{-1})$ for PI (a) and TI (b) for a pixel size of 3μm and λ=515nm, and its superposition on the power spectrum of the corresponding hologram (c) and (d).

Figure 6a shows that the use of a rectangular aperture in parallel illumination does not reduce the $K_z$ range and, in consequence, neither the axial resolution. For parallel illumination the maximum value of $K_z$ is zero and occurs at the center of the spectrum, while the minima values occurs at the four corners. For tilted illumination, the maximum has a non-zero value, $K_{z,max} = k(1 - \cos\sigma/2)$ and the minima values (smaller than with a parallel illumination) can be found at the right corners. Thus, a comparison of Figure 6a and 6b reveals the improvement obtained with the tilted illumination when there is not any aperture.

Figure 6 shows a wider range of $K_z$ with PIRA than for TIRA, which suggests a better axial resolution. However, experimental results will prove that a clear advantage is obtained with a TIRA configuration. The reason is the low intensity at the corners of the spectrum for particle fields. The particle scattering usually presents a high forward main lobe that appears around the illumination wave vector $\boldsymbol{k_i}$. Consequently, the particle scattering results in an effective aperture of smooth edges, whose size will decrease with the particle diameter. To minimize the problem, we have chosen particles whose size is around 3μm (i.e. one pixel). Nevertheless, the hologram power spectrum (figures 3c, 3d and 4b) show that their scattering decreases dramatically near the four corners. The superposition of the power spectrum obtained for a PIWA and a TIWA holograms with the corresponding $K_z$ maps (figure 6c and 6d) suggests that only the frequencies below a certain value are appropriately measured. Assuming the

intensity allows the whole $\xi$ and $\eta$-axis to be measured, so that $\xi^2 + \eta^2 < 0.5/pix$. Within that assumption, figure 5-bottom shows the actual maximum and minimum $K_z$ values for each configuration.

In this case, the corresponding axial resolution for PIRA and TIRA configuration are:

$$R_z^{PIRA} = \frac{2\pi}{\Delta K_z} = \frac{\lambda}{1-\cos(\sigma)} = 8\,pix^2 / \lambda \qquad \textbf{(3)}$$

$$R_z^{TIRA} = \frac{2\pi}{\Delta K_z'} = \frac{\lambda}{[1-\cos(\sigma)]+[1-\cos(\sigma/2)]} \qquad \textbf{(4)}$$

Eq. 3 and Eq. 4 show that $R_Z^{TIRA}$ is smaller than $R_Z^{PIRA}$ for any value of $\sigma$. Particularly, for small numerical apertures, when $1-\cos(\sigma) \approx \sigma^2/2$, the ratio $R_Z^{TIRA}/R_Z^{PIRA} \approx 0.8$. For bigger values of $\sigma$, this ratio will be even smaller.

Let us note that without rectangular aperture, the information at the Fourier plane from the real and virtual image will be mixed and overlapped. Then, figure 6 can only be considered a true representation of $K_z$ if the twin image is removed in another way and without modifying the frequency spectrum.

If we consider now a symmetrically tilted illumination, the obtained $K_z$ values are very similar. Therefore, a double-tilted illumination (DTI) does not improve the axial resolution. Furthermore and even for the RA configuration, the different contributions will appear overlapped on the frequency spectrum, and the crossed terms can produce duplicated particle images during the particle field image reconstruction.

The overlapping will disappear by using a square aperture, SA (figure 7). Figure 7a shows the $K_z$ values that can be measured with this DTISA configuration. The computed $K_z$ for each of the two illuminations appear in one quadrant of the power spectrum. From a comparison of Figs. 7b) and 7c) with Figs 5a) and 5c), it can be concluded that $\Delta K_y'' = \Delta K_x$ and $\Delta K_x'' = 2\Delta K_x'$. Therefore, $R_y^{DTISA} = 2pix$, and $R_x^{DTISA} \approx 1pix$, as if a rectangular aperture has been placed horizontally. On the other hand, to find the full range of $K_z$ both sections (Fig 7b and 7c) should be taken into account. Moreover, from a comparison of figure 6d and 7a we can conclude that $\Delta K_z'' = \Delta K_z'$, and the same resolution should be expected in the Z-direction with a DTISA and a TIRA configuration: $R_Z^{DTISA} = R_Z^{TIRA}$.

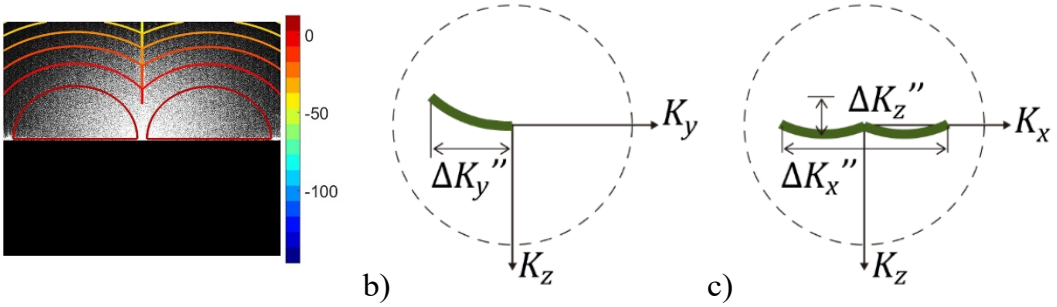


a) b) c)

Fig. 7. Map of $K_z$ $(mm^{-1})$ superposed on the power spectrum (a) and measurable sensitivity vector: YZ section (b) and XZ section (c) for the DTISA configuration.

## 4. Experimental validation

The effect of an aperture and a parallel, tilted or double-tilted illumination beam is investigated with a test object made with a standard microscope slide and 3µm particles sprinkled on its surface. A 515nm DPSS laser beam is guided through an optic fiber. The output tip is located at the focal plane of a collimating lens. The lateral position of the fiber end is adjusted to change from parallel to tilted illumination in our experimental set-up. A fiber-coupling device with two output tips is used for double-tilted illumination (figure 8). Two crossed polarizing plates are located near the end of each fiber to minimize the interference between both illuminations. The residual interference appears as two weak local maxima near the limits of the horizontal axis in the Fourier Transform of the DTI recordings. The position of these peaks has been used to determine the angular separation between both illuminations with high accuracy.

The angle of the illumination beam, actually the reference beam, should be taken into account during the numerical reconstruction. For instance, to combine multiplexed recording, each object wave is computed separately using the corresponding reconstruction wave and the Angular Spectrum method [5]. The overlapped area is blocked to eliminate the crossed interference terms. The final particle image field is computed by the coherent addition of each object wave after multiplying by the conjugated illuminating wave, as in Optical Diffraction Tomography imaging [16, 20].

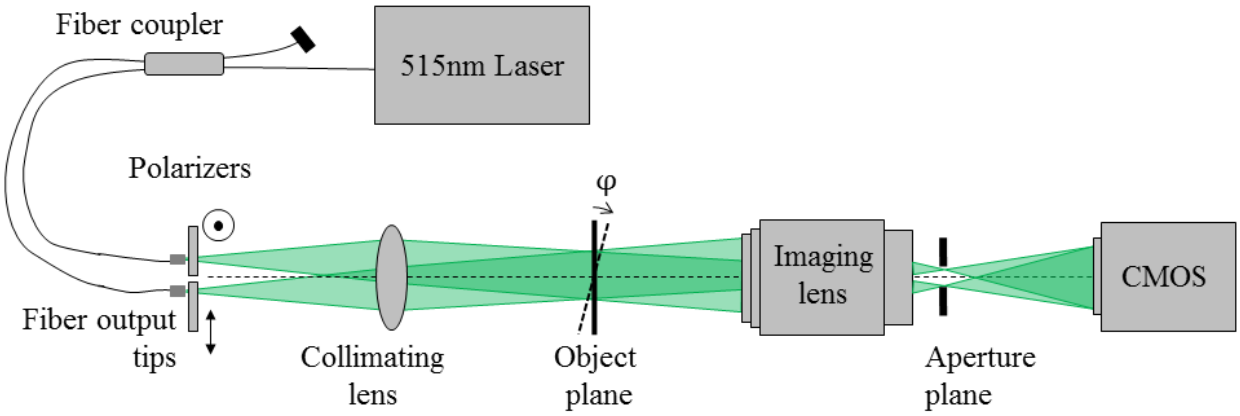


Fig. 8. Schematic drawing of the experimental set-up.

Holograms of these five orientations were recorded with all the possible configurations (PIWA, PIRA, TIWA, TIRA, DTIWA, DTIRA and DTISA). A region of 6.1mm×7.2mm is recorded in a 2160×2560 CMOS sensor so that the pixel size in the object space is $pix = 2.83\mu m$. Around 2450 particles can be found in the field of view of each hologram. To control the particle displacement, the microscope slide was rotated, so that its normal direction makes angles of $\varphi = -5^0, 0^0, 5^0, 10^0, 15^0$ with the optical axis. Particles are between 0.5mm and 3.0mm away from the best-focused plane. The rotation axis is outside the field of view, so

that the axial displacement Δz ranges from 0.05mm to 0.70mm. In this way, the particles are always slightly defocused and there are not particles with zero-displacement. These two conditions remove the problems of position sign uncertainty and biased Δz measurements respectively, which are very relevant when the twin image is present [9]. These are the best working conditions for all the WA and the DTIRA configurations (coloured in red in figure 9) while being not relevant for the other three configurations (coloured in blue in figure 9).

Reconstructed particle images appear as clear intensity 3D local maxima. According to equation (3) and (4), the theoretical axial resolution of $R_z^{PIRA} = 124\mu m$ and $R_z^{TIRA} = 99\mu m$ for our experiments. In order to avoid an unnecessary increase on the computation time and memory requirements, the particle images are located in two steps [4]: first a sampling in the observation direction of *pz*=0.12mm has been chosen. The reconstructed volume is divided into equally sized rectangular parallelepipeds ($24 \times 24pix^2 \times 3.60\ mm$) where the absolute maximum is calculated. In a second step, the complex amplitude of the reconstructed image is computed around these positions in smaller volumes, sampling every *pz*=0.04mm. The final position is obtained from fitting the intensity data to a quadratic function of the coordinates. In the lateral coordinates sub-pixel resolution is obtained, and for the same reason, the error in the particle axial position is smaller than the theoretical axial resolution.

Then, the 3D particle positions are adjusted to a planar distribution. Thus, for each lateral position (xy-coordinates) the nominal axial position (z-coordinate) should be on this plane. The difference from the measured and nominal axial position, $z_{error}$, is computed for the first four holograms. The histograms of $z_{error}$and its standard deviation (STD) are presented in figure 9 (left column) and their standard deviations (STD) are listed in table 1.

These particles are tracked with a cross-correlation between the 3D intensity distribution reconstructed from one hologram and the next one around each particle position. The dimensions of the interrogation volumes are $64 \times 64pix^2 \times 2.0\ mm$. A threshold removes the background noise below an adaptive value: twice the standard deviation of the intensity within the interrogation volume. This threshold ensures the defocused particle field does not introduce bias in the displacement measurements, which is essential in the configuration where the twin image is present [8].

The 3D measured displacements between two consecutive holograms are also fitted to a linear dependence with XY-coordinates, and therefore, the nominal $\Delta z$ can be computed from the lateral position of the particles. The histograms of the difference from the measured and nominal axial displacement, $\Delta z_{error}$ , and their STD are shown in figure 9 (central column) and table 1 respectively.

The gradient of the displacement can affect the results, since a big interrogation volume is required. Thus, once the displacement of each particle is roughly known, a second cross-correlation can be computed with a reduced interrogation window around the expected particle position. In this way, the background noise coming from the unfocused particle images will affect much less the displacement measurements. The interrogation volume reduction would improve the measurements by itself, but it also allows using a complex amplitude cross-correlation that provides a sharper correlation peak [28, 4]. Figure 9 (right column) and table 1 show the histograms of the newly computed $\Delta z'_{error,}$ and their STD with a complex

amplitude cross-correlation and an interrogation window of $10 \times 10pix^2 \times 1.0\ mm$.

Several conclusions can be extracted from the results shown on figure 9 and table 1, where the best results are bold highlighted in bold. As in the lateral coordinates, the axial displacement measurements present smaller error than the axial position. The main performance differences are found in the measurement of the axial displacement with a first cross-correlation. After the second cross-correlation, the histograms are shaper and the STD is reduced by a factor of more than two for all the configurations. Thus, different scales are used for each column of figure 9.

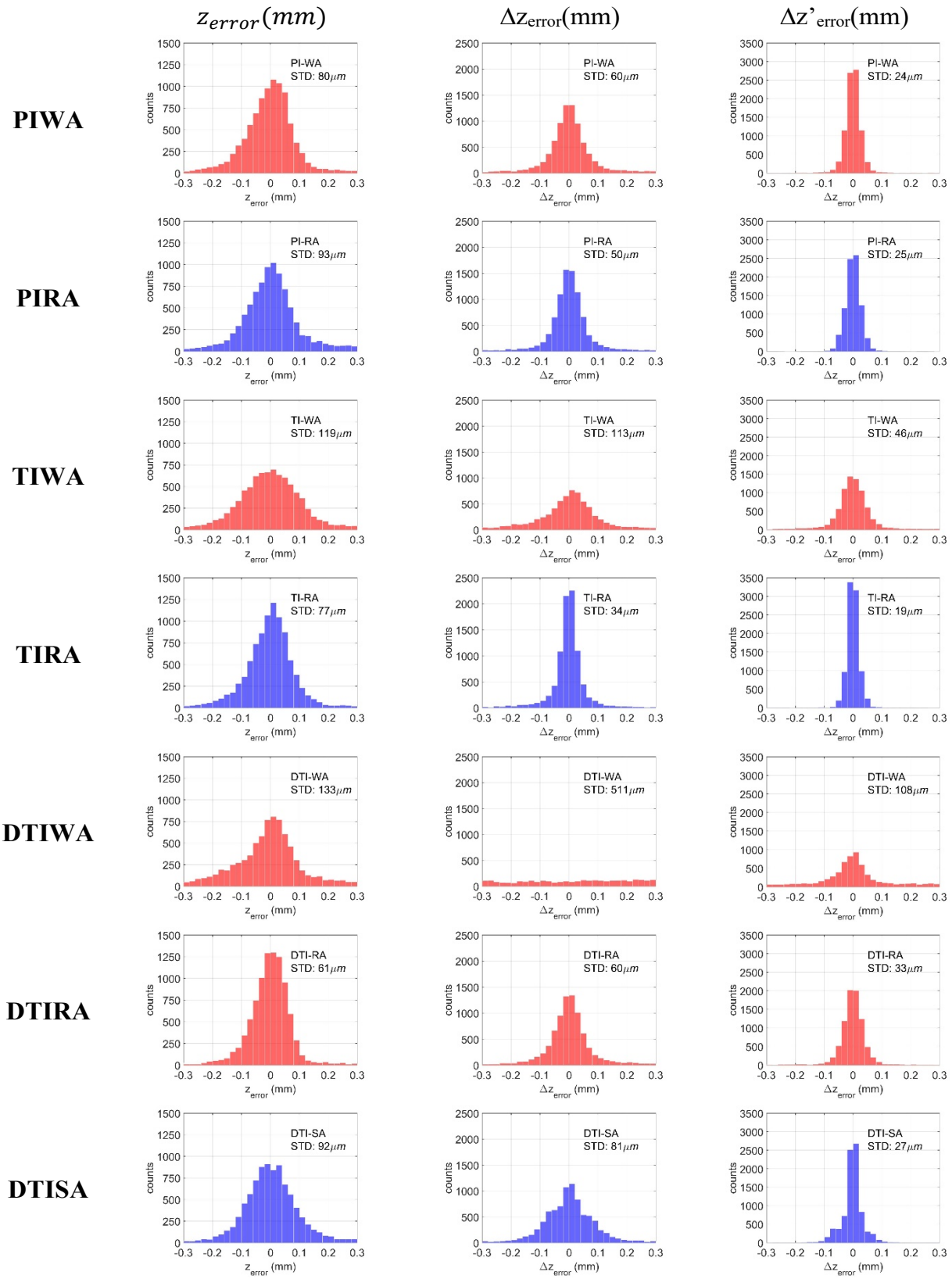


Fig. 9. Histograms of errors in axial positions ($z_{error}$f) and displacements ($\Delta z_{error}$ and $\Delta z'_{error}$) for parallel, tilted and double-tilted illumination and different apertures.

Table 1. STD values for errors in axial positions (z) and displacements (Δz and Δz') for parallel, tilted and double-tilted illumination and different apertures.

| | **STD-z (μm)** | **STD-Δz (μm)** | **STD-Δz' (μm)** |
|---|---|---|---|
| **PIWA** | 80 | 60 | 24 |
| **PIRA** | 93 | 50 | 25 |
| **TIWA** | 119 | 113 | 46 |
| **TIRA** | 77 | **34** | **19** |
| **DTIWA** | 133 | 511 | 108 |
| **DTIRA** | **61** | 60 | 33 |
| **DTISA** | 92 | 81 | 27 |

Comparing with the other configurations TIWA and DTIWA show disappointing results, both doubled the STD of the best-performance configuration. DTIWA does not provide a valid estimation of the displacement field after the first cross-correlation. The nominal z-positions have been used to facilitate the second cross-correlation and, still the performance is very poor comparing with other options. The analysis of the measurable $K_z$ (figure 7b) does not justify it. It seems that the background noise, which comes from the unfocused twin particle fields, hinders the particle location and tracking. The constraints imposed on our experiments and the analysis strategies (an intensity threshold on the particle image and a reduced interrogation window) used to remove the unwanted unfocused images were enough for the standard PIWA configuration, which shows a nice performance. However, with a tilted illumination, the unwanted unfocused images are shifted laterally from their focused twins, and they affect the neighbour particles that may have a different brightness.

As expected, PIRA shows similar performance than PIWA but without having the minimum defocusing distance and displacement requirements.

DTIRA does present the best performance in the particle location, although its use imposes a minimum defocusing distance and displacement that it is not necessary with TIRA configuration. The presence of the double image increases the uncertainty and can help to locate the particles, but it underestimates the displacements near zero [9].

DTISA results do not match the performance of TIRA. The reason can be found in the lost overlapped area between the twin images in the Fourier domain and any calibration errors in the multiplexing set-up. Overall TIRA shows the best axial resolution for location and displacements. The effect of the intensity distribution of the forward scattering is crucial to justify this performance, as suggested in section 3. TIRA is particularly robust for big interrogation window and displacement gradients. Furthermore, it is not affected by any restrictions on the focus distance or the displacements that can be measured.

## 5. Conclusions

For DIH, the aperture size can be directly related to the lateral resolution, but the illumination direction has to be taken into account in order to obtain the axial resolution. The dependence of the axial resolution for several digital in-line holography configurations has been stated. A two-dimensional map of the measurable axial spatial frequencies has been proposed to visualize the effect of an aperture or a small tilt in the illumination. It has been shown that multiplexing in-line recordings with the same wavelength does not improve the axial resolution.

A theoretical analysis of the measured spectral components of the object shows that the uncertainty in the determination of the axial particle position can be reduced when the illumination beam is slightly tilted. For an in-line configuration, the sensor pixel size and the magnification of the imaging system determine the maximum tilt of the illuminating beam, and consequently the axial resolution. The forward particle scattering behaves as an effective aperture, which should be also taken into account, especially for big particles.

The theoretical limits on the axial spatial resolution have been obtained for the parallel illumination and rectangular aperture (PIRA), tilted illumination and rectangular aperture (TIRA) and double tilted illumination with square aperture (DTISA) configurations, which are not affected by the twin image problem that can hinder the frequency information. This analysis suggests that the axial resolution of TIRA should be similar to the DTISA and improve those expected from a PIRA configuration. One-wavelength in-line multiplexed recordings do not show the advantage they have demonstrated in off-axis configurations, due to the restriction of using small angles between the illumination and the observation directions.

Several experiments have been carried out with a planar object with one-pixel particles, whose position and displacement are easily controlled. The recorded particle field has a minimum defocus distance and a minimum displacement. These constraints, together with the use of an intensity threshold and a reduced interrogation window, should remove the unwanted twin image expected for the standard DIH configuration (PIWA). Our experiments show that, even within this restriction, the use of the full aperture does not show better resolution than the configurations with an appropriate aperture, such as PIRA or TIRA.

It has been demonstrated that, with an in-line holographic set-up, one single tilted illumination with a rectangular aperture (TIRA) outperforms any other configuration. TIRA improves more than a 17% the position and a 32% the displacements measurements obtained with a PIRA configuration. It was also confirmed that multiplexing in-line recordings does not improve the axial resolution. A double tilted illumination with rectangular aperture configuration (DTIRA) shows a 20% improvement with respect to TIRA in the location of the particles, but in the measurement of the displacement, it duplicates the error obtained with TIRA. A tilted illumination and a rectangular aperture configuration is particularly robust for big displacement gradients, and it does not require any constraint on the particle position or displacement value.

## Funding

Spanish Ministerio de Economía y Competitividad (MINECO) and EuropeanCommission FEDER Program (DPI2016-75791-C2-2-P/1-P); Gobierno de Aragón- Feder 2014-2020 "Construyendo Europa desde Aragon" (E44_17R); Marina Gómez Climente has been supported by BES-2017-080924.

## References

1. Arroyo MP, Hinsch KD, Recent Developments of PIV towards 3D Measurements. Ed. A Schroder, C.E. Willert, Springer, New York, 2008, p. 127.
2. Katz J, Sheng J, Applications of holography in fluid mechanics and particle dynamics. Annu Rev Fluid Mech 2010;42:531.
3. Memmolo P, Miccio L, Paturzo M, Di Caprio G, Coppola G, Netti P A, and Ferraro P. Recent advances in holographic 3D particle tracking. Adv Opt Photon 2015;7:713
4. López AM, Lobera J, Andrés N, et al Arroyo MP, Palero V, Sancho I, Vernet A, Pallarés J. Advances in interferometric techniques for the analysis of the three-dimensional flow in a lid-driven cylindrical cavity. Exp Fluids 2020;61:10.
5. Goodman JW. Introduction to Fourier Optics, McGraw-Hill Series in Electrical and Computer Engineering, 1996.
6. Rastogi PK. Holographic Interferometry. Principles and methods. Springer-Verlag, Berlin 1994.
7. Kreis T. Handbook of holographic interferometry. Wiley-VCH, Bremen, 2005
8. Ooms T, Koek W and Westerweel J. Digital holographic particle image velocimetry: eliminating a sign-ambiguity error and a bias error from the measured particle field displacement. Meas Sci Technol 2008;19:074003
9. Palero V, Lobera J, Andrés N and Arroyo MP. Shifted knife-edge aperture digital in-line holography for fluid velocimetry. Opt Lett 2014;39:3356-59
10. Denis L, Fournier C, Fournel T, and Ducottet C. Numerical suppression of the twin image in in-line holography of a volume of micro-objects. Meas Sci Technol 2008;19:074004
11. Bryngdahl O and Lohmann A. Single-Sideband Holography. J Opt Soc Am 1968;58:620-624
12. Ramirez C, Lizana A, Iemmi C and Campos J. Method based on the double sideband technique for the dynamic tracking of micrometric particles. J Opt 2016;18:065603
13. Lobera J, Palero V, Roche EM, Gómez Climente M, López Torres AM, Andrés N, Arroyo MP. Multiplexed two in-line holographic recordings for flow characterization in a flexible vessel. Proc. SPIE 2017;10333:103330J
14. Latychevskaia T, Gehri F, and Fink HW. Depth-resolved holographic reconstructions by three-dimensional deconvolution. Opt. Express 2010;18, 22527-22544
15. Latychevskaia T, Fink HW. Holographic time-resolved particle tracking by means of three-dimensional volumetric deconvolution. Opt. Express 2014;22, 20994-21003
16. Coupland JM and Lobera J. Holography, tomography and 3D microscopy as

linear filtering operations. Meas Sci Technol 2008;19:074012.

17. Elsinga GE, Scarano F, Wieneke B, van Oudheusden BW. Tomographic Particle Image Velocimetry. Exp Fluids 2006;41:933-947

18. Lobera J and Coupland JM. Optical diffraction tomography in fluid velocimetry: the use of a priori information. Meas Sci Technol 2008;19 074013

19. Memmolo P, Finizio A, Paturzo M, Miccio L, Ferraro P. Twin-beams digital holography for 3D tracking and quantitative phase-contrast microscopy in microfluidics. Opt Express 2011;19:25833-25842

20. Saglimbeni F, Bianchi S, Lepore A, and Di Leonardo R. Three-axis digital holographic microscopy for high speed volumetric imaging. Opt Express 2014;22: 13710-13718

21. Meng H and Hussain F. In-line recording and off-axis viewing technique for holographic particle velocimetry. Appl Opt 1995;34:1827-1840

22. Lai S, Kemper B, Bally G. Off-axis reconstruction of in-line holograms for twin-image elimination. Opt Commun 1999;169:37-43

23. Ooms T, Koek W, Braat J and Westerweel J. Optimizing Fourier filtering for digital holographic particle image velocimetry. Meas Sci Technol 2006;17(2)

24. Wolf E. Three-dimensional structure determination of semi-transparent objects from holographic data. Opt Commun 1969;1:153-156

25. Ruiz P, Huntley J, Coupland J. Depth-resolved imaging and displacement measurement techniques viewed as linear filtering operations, Exp Mech 2011;51:453-465.

26. Born M, Wolf E, Principles of Optics, 7th Ed. Cambridge University Press 2013

27. Latychevskaia T. Lateral and axial resolution criteria in incoherent and coherent optics and holography, near- and far-field regimes. Appl Opt 2019;58:3597-3603

28. Wormald SA, Coupland J. Particle image identification and correlation analysis in microscopic holographic particle image velocimetry. Appl Opt 2009;48:6400-6407